Mode-Selective Acoustic Spectroscopy of Trigonal Piezoelectric Crystals

Ward L. Johnson, Carlos F. Martino, Sudook A. Kim, and Paul R. Heyliger

Abstract—A noncontacting electromagnetic-acoustic-resonance technique is presented for generating and detecting vibrational modes with prescribed symmetries in piezoelectric trigonal crystals with cylindrical geometry. This technique provides the experimental basis for determining all elastic constants from a single specimen, while overcoming difficulties in mode identification that can occur in traditional resonant-ultrasound spectroscopy. Narrow-band tone-burst excitation and piezoelectric coupling are employed with various geometrical configurations of electrodes near the surface of a quartz specimen. The geometries of the specimen and plates include all of the symmetry elements of the crystallographic point group, which enable selection of the irreducible representation of excited vibrational modes simply by switching electrical leads to the electrodes.

I. INTRODUCTION

RESONANT ultrasound spectroscopy (RUS) has been used extensively for determining the elastic constants of materials through least-squares fitting of the resonant frequencies to Ritz calculations [1]. In the past few years, Ritz analysis that includes piezoelectric terms in the equation of motion has been shown to enable simultaneous determination of not just elastic constants, but also piezoelectric coefficients from RUS measurements on piezoelectric crystals [2]–[6]. The application of this method to piezoelectric crystals presents advantages over traditional methods, which involve separate acoustic pulse-echo and piezoelectric measurements on more than one specimen. In addition to reducing the time of measurements and specimen fabrication, it eliminates uncertainties arising from variations in the material of multiple specimens (due, for example, to inhomogeneity of a crystal boule). For measurements as a function of temperature, it eliminates uncertainties arising from differences in temperature during multiple runs, which can affect the determination of temperature-independent cuts of resonators for frequency-control applications. These issues of accuracy and material homogeneity are particularly relevant today, since a number of innovative piezoelectrics, including langatate and materials with similar crystal structure, have emerged as

candidates for replacing quartz in some applications, and the properties of these crystals and optimal methods for growing them are not yet established.

In this report, we present methods that extend the metrology of resonant acoustics on trigonal piezoelectric crystals by implementing selective excitation of modes of prescribed symmetry with noncontacting transduction. These methods address issues that limit the accuracy of conventional contacting RUS measurements and Ritz analysis of these measurements. First, noncontacting transduction reduces perturbations of the boundary conditions that affect the resonant frequencies and the corresponding accuracy of the determination of material constants. This is an issue particularly with respect to accurately determining piezoelectric coefficients [3], [7]. Note that, although forces always must be present to support a specimen when either contacting or noncontacting transduction is employed, the magnitude of the perturbation of the acoustic boundary conditions depends also on the acoustic impedance of the supporting material. Highly mismatched low-impedance supporting material can be employed with noncontacting transduction, but such material is incompatible with the need to effectively transmit acoustic energy between a specimen and contacting piezoelectric transducers in conventional RUS. The second issue that is addressed with the methods presented here is the often challenging task of identifying modes in Ritz analysis. The correct one-to-one correspondence must be established between measured and calculated modes before Ritz analysis is undertaken, or the fitting algorithm may converge to an incorrect local minimum. Therefore, although conventional RUS has the advantage of providing the frequencies of many resonant modes with a variety of symmetries, it has the corresponding disadvantage of requiring fairly accurate initial values for the elastic constants in the inverse calculation. As summarized by Ogi *et al.* [8], various researchers have attempted to address this problem by changing specimen dimensions, switching assignments of modes in the inversion algorithm, or changing positions of transducers. Ogi *et al.* [4], [6], [9], [10] have used laser-Doppler interferometry to provide separate information on the displacement patterns. This approach is particularly powerful because it maintains the advantage of providing information on many modes of various symmetry. However, in cases where measurements must be performed relatively rapidly or access to the specimen is limited, separate measurement of displacements may not be practical. A simpler approach to mode identification is spatial selectivity in transduction. Spatial selectivity is achieved naturally

W. L. Johnson, C. F. Martino, and S. A. Kim are with the Materials Reliability Division, National Institute of Standards and Technology, Boulder, CO 80305 (e-mail: wjohnson@boulder.nist.gov).

P. R. Heyliger is with the Department of Civil Engineering, Colorado State University, Fort Collins, CO 80523.

with electromagnetic-acoustic resonance (EMAR) employing Lorentz-force coupling [11], and this has been used to excite modes with specific symmetries in metallic parallelepipeds for Ritz analysis [8], [12]. In a direct comparison of Ritz inversion analysis applied to EMAR and RUS data on monocrystalline copper, Ogi *et al.* [8] found that the two methods yielded essentially the same elastic constants, despite fewer resonant peaks in EMAR. Because of the ability to identify modal symmetries, the inversion analysis with EMAR data was found to be much more robust than that with RUS data. Inaccuracies of tens of percent in the initial guesses for the elastic constants in the EMAR analysis had no effect on the convergence of the calculations, while inaccuracies of $\sim 1\%$ or less in the initial guesses for the RUS analysis resulted in convergence to an incorrect local minimum.

The acoustic-resonance method that we present here for application to piezoelectric crystals is similar to previous EMAR methods in the sense that it uses noncontacting distributed transduction to selectively couple to modes with prescribed symmetries. It employs direct piezoelectric coupling through a switchable pattern of electrodes surrounding a trigonal crystal in the form of a cylinder. The use of a cylindrical geometry, with the trigonal axis oriented along the cylindrical axis of the specimen, maintains all of the symmetry operations of the crystallographic point group and, therefore, allows complete categorization of the modes according to group theory. Correspondingly, the Ritz eigenvalue problem is divided into submatrices of minimal size [13], [14].

Although one of the intended applications of the techniques presented here is the simultaneous determination of elastic constants and piezoelectric coefficients, the inclusion of piezoelectric effects in an analysis of the vibrational modes is not necessary for demonstrating methods of coupling to acoustic modes with prescribed symmetries, as described below. Therefore, piezoelectric terms in the equations of motion are not included here in the Ritz analysis of spectra.

II. Specimen Geometry and Crystallographic Symmetry

The specimen is a monocrystal of quartz that was ground into the shape of a cylinder with a radius of 5.389 ± 0.001 mm and a height of 15.064 ± 0.001 mm. The crystallographic space group of quartz is $P3_121$, and the corresponding trigonal point group is 32 in the international notation, or D_3 in the Schoenflies notation. The three-fold crystallographic axis was oriented along the cylindrical axis of the specimen.

The lack of inversion symmetry of D_3 is reflected in the piezoelectric character of quartz. Exact analysis of the vibrational modes must include piezoelectric terms, in addition to elastic terms, in the equation of motion. However, the piezoelectric coefficients of quartz are not large (compared to those of other materials, such as lithium niobate,

that are commonly used for acoustic transducers) and introduce only slight perturbations to the displacement patterns and resonant frequencies of a specimen. Therefore, for the purposes of demonstrating mode selectivity of transduction, we consider the vibrational modes entirely within linear elastic theory. Since linear elastic vibrations are insensitive to a lack of inversion, the inversion operator can be included in the analysis of symmetries of vibrational modes, and the D_{3d} point group becomes elastically equivalent to the trigonal point group with the greatest number of symmetry operations, D_{3d} [14].

Fig. 1 depicts an object with symmetry including the group elements of D_{3d}, which are defined to be spatial transformations that leave the appearance of the object unchanged. In addition to the axes shown in the figure, axis $\hat{d}$ is defined to be in the same plane as $\hat{x}$ and $\hat{f}$ and halfway between them on the back side of the object. The group elements include a rotation of $2\pi/3$ about $\hat{z}$ (denoted by C_{3z}); a rotation of $-2\pi/3$ about $\hat{z}$ (denoted by C_{3z}^{-1}); rotations of π about $\hat{x}$, $\hat{f}$, and $\hat{d}$ (C_{2x}, C_{2f}, C_{2d}, respectively); inversion (I); the identity operation (E, no spatial transformation); and the products of inversion and rotations (IC_{3z}, IC_{3z}^{-1}, IC_{2x}, IC_{2f}, IC_{2d}).

There are six group-theoretical irreducible representations (IRs) of the crystallographic point group D_{3d}, as shown in Table I: four one-dimensional representations, labeled A_{1g}, A_{2g}, A_{1u}, and A_{2u}, and two two-dimensional representations, labeled E_g and E_u [15]. The subscripts "g" or "u" indicate that the corresponding vibrational modes (basis functions for the IRs) are, respectively, even or odd under inversion. The column labels in Table I designate the classes, which are defined to include the following symmetry elements [15]:

$$
\begin{aligned}
C_1 &\equiv E, \\
C_2 &\equiv C_{3z}, C_{3z}^{-1}, \\
C_3 &\equiv C_{2x}, C_{2f}, C_{2d}, \\
C_4 &\equiv I, \\
C_5 &\equiv IC_{3z}, IC_{3z}^{-1}, \\
C_6 &\equiv IC_{2x}, IC_{2f}, IC_{2d}.
\end{aligned}
\tag{1}
$$

The focus of this paper is only on vibrational modes that are basis functions for the one-dimensional representations. Within this context, the interpretation of the values ("characters") in Table I is simple. A vibrational displacement pattern that forms a basis for a particular representation is unchanged by application of a symmetry operation that has a character of 1, and it is reversed in sign by application of a symmetry operation that has a character of -1.

III. Transducers

Direct piezoelectric transduction was employed to excite vibrations in the specimen from radio frequency (RF) tone bursts applied to noncontacting electrodes, and the inverse effect was employed to detect resonant vibrations
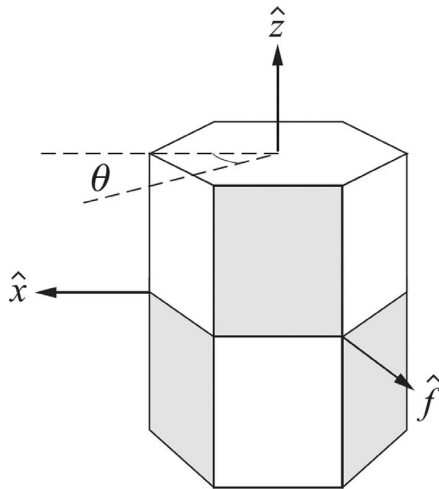
Fig. 1. Symmetry and definitions of axes for an object belonging to the D_{3d} point group. An additional two-fold rotation axis on the back side of the image (not shown) is in the plane of $\hat{x}$ and $\hat{f}$ and halfway between them.

TABLE I
IRREDUCIBLE REPRESENTATIONS, CLASSES OF SYMMETRY TRANSFORMATIONS, AND CORRESPONDING CHARACTERS FOR THE D_{3d} POINT GROUP.

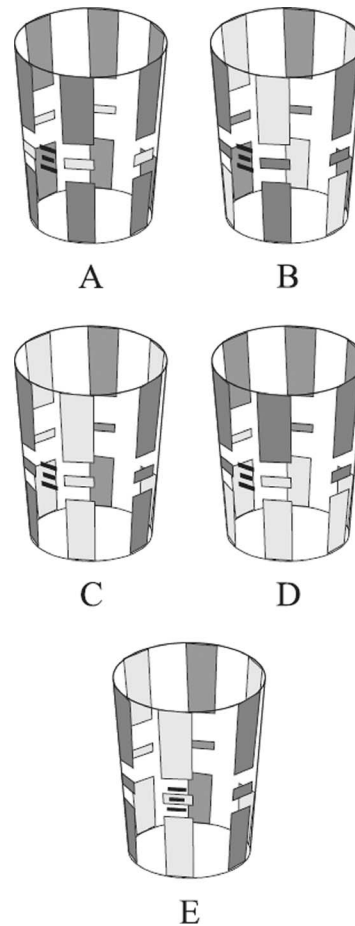|	C_1	C_2	C_3	C_4	C_5	C_6
A_{1g}	1	1	1	1	1	1
A_{2g}	1	1	−1	1	1	−1
A_{1u}	1	1	1	−1	−1	−1
A_{2u}	1	1	−1	−1	−1	1
E_g	2	−1	0	2	−1	0
E_u	2	−1	0	−2	1	0

Fig. 2. Configurations of electrodes surrounding the cylindrical specimen. The voltages on the dark and light electrodes have opposite polarity. The symbol Ξ corresponds to a two-fold symmetry axis.

of the specimen following excitation. This method is referred to here as EMAR because it employs noncontacting electromagnetic coupling to resonant acoustic modes, although this acronym previously has been applied only to techniques employing Lorentz-force or magnetostrictive coupling.

As shown in Fig. 2, a single geometric configuration of electrodes was used, and several different patterns of voltages, indicated by the shading of electrodes, were used to selectively couple to modes with prescribed symmetries. The electrodes were fabricated from copper tape mounted on the outer surface of a hollow plastic/fabric composite cylinder with an inner diameter of 10.9 mm, a wall thickness of 1.1 mm, and a length of 22 mm. The specimen was centered inside this cylinder with its base resting on a mica washer. Mica was chosen for the support because acoustic coupling and transmission through this material are low. The symbol Ξ in each image of the figure corresponds to a two-fold symmetry axis of the specimen ($\hat{x}$, $\hat{f}$, or $\hat{d}$ in Fig. 1).

The electrodes depicted in Fig. 2 are driven with RF tone bursts, as described in the next section, with the lightly and darkly shaded electrodes having opposite polarities. For each of the configurations, the instantaneous

potentials are either unchanged or inverted under each of the symmetry transformations of (1), so that the potentials form bases for the one-dimensional IRs. This also is true of the electric fields and piezoelectrically induced strain fields. Appendix A presents an analysis of the symmetries of the potentials, electric fields, and strain fields for each of the configurations, and the results of this analysis are summarized in Table II.

The particular configurations of Fig. 2 certainly are not the only ones that could be employed to produce potentials and fields with the general symmetries listed in Table II. For example, the IRs would be unchanged, except for that of configuration A, if the central ring of smaller electrodes were eliminated.

The transducers shown in Fig. 2 couple to three of the four one-dimensional representations of D_{3d}. Our focus is primarily on configurations *A-D*, between which one can switch simply by switching the connections of the electrode leads, since the crystallographic orientation of the specimen is the same in these configurations. Configuration *E*, which involves an axial rotation of the specimen relative to the other configurations, was used primarily to facilitate initial alignment of the two-fold axis of the specimen, as described below.

TABLE II
SYMMETRIES OF THE ELECTRIC POTENTIALS V, ELECTRIC FIELDS $\vec{E}$, AND PIEZOELECTRICALLY INDUCED STRAIN FIELDS S FOR EACH OF THE ELECTRODE CONFIGURATIONS.

Configuration	V	$\vec{E}$	S
A	A_{1g}	A_{1g}	A_{1u}
B	A_{1g}	A_{1g}	A_{1u}
C	A_{2u}	A_{2u}	A_{2g}
D	A_{2u}	A_{2u}	A_{2g}
E	A_{1u}	A_{1u}	A_{1g}

IV. EXPERIMENTAL AND ANALYTICAL TECHNIQUES

The electronic apparatus for EMAR measurements is based on a RITEC RAM-5000 (SNAP; Ritec, Inc., Warwick, NJ)[1], which includes a gated amplifier and a phase-sensitive receiver that are synchronized using a continuous sine wave [16]. The output of the gated amplifier is a narrow-band sinusoidal tone burst, typically 1 to 5 ms in duration, that drives the electrodes of the transducer in one of the configurations described above. The receiver is connected to the electrodes through an active diplexer that breaks the connection during the driving tone burst to protect the receiver. With a driving frequency ω_o near the frequency ω_r of an acoustic mode, the ringdowns of RF voltages induced on the electrodes after the driving tone burst are processed by the receiver to produce two simultaneous outputs V_n ($n = 0, 1$), given by

$$V_n = A \exp(-\alpha t) \cos\left[(\omega_o - \omega_r)t - \frac{n\pi}{2} - \phi\right], \quad (2)$$

where α is the acoustic damping, ϕ is a constant phase shift introduced in the electronics, and A is a constant dependent on the gain of the receiver and the strength of the RF signal. Apart from the phase shift ϕ, the outputs with $n = 0$ and $n = 1$ are proportional to the instantaneous magnitudes of the signal that are, respectively, in phase and out of phase with the reference sine wave (analogous to the outputs from a lock-in amplifier).

The digitized outputs of the receiver were analyzed by a computer in real time with two different methods. For the purpose of acquiring approximate spectra over a broad range, the integral of $(V_0^2 + V_1^2)^{1/2}$ over the ringdown (proportional to the time-integrated RF signal amplitude) was calculated for each driving frequency in a computer-controlled series between 0.2 MHz and 1.0 MHz with 100 Hz steps. For the purpose of accurately determining each individual resonant frequency, the driving frequency was set near the resonance, a complex Fourier transform was performed of V_0 and V_1, and the frequency of the peak in this transform was recorded.

To align the crystallographic two-fold rotation axes of the specimen for EMAR measurements, the A_{1g} mode with a calculated frequency near 0.32 MHz was employed. This is the only mode with a significant peak height observed below 0.600 MHz in configuration E. To set up this configuration, the specimen was rotated about its axis to find the position at which the height of this peak was maximized. In a similar manner, the height of this peak was minimized to set up configurations A, B, C, and D. This procedure for configurations A–D achieves accurate alignment of the two-fold axis more easily than directly maximizing A_{1u} or A_{2g} modes, because the magnitude of coupling to these modes is at the maximum of an approximate sinusoidal angular dependence (with zero slope) in these configurations. Once the two-fold-axis alignment was accomplished for configurations A–D, the position of the crystal was left undisturbed during measurements in these configurations, and only the polarities of the electrodes were changed to generate the different symmetries of electric fields.

Conventional RUS also was used to measure resonant frequencies of the specimen. These measurements employed two piezoelectric transducers that supported the specimen by mechanical contact on opposite edges. The frequencies determined from RUS were fit to Ritz calculations in cylindrical coordinates with the elastic constants as adjustable parameters. This inversion analysis was based on the formulation of the Ritz method in cylindrical coordinates derived by Heyliger and Johnson [13], [14].

A demonstration of the degree to which the EMAR configurations of Fig. 2 selectively couple to modes of particular symmetry is somewhat of a "chicken before the egg" challenge. This is accomplished here by 1) performing RUS measurements (which provide no direct information on symmetry); 2) performing a forward Ritz calculation using published elastic constants of quartz; 3) estimating, by inspection, the range of lower frequencies over which there is a one-to-one correspondence of the RUS and forward-Ritz frequencies; 4) performing inverse Ritz analysis of the RUS data over this frequency range to confirm the one-to-one correspondence, provide a more accurate comparison of frequencies, and clearly identify modal symmetries; 5) aligning the two-fold axis of the specimen according to the EMAR configurations of Fig. 2 with the resonant amplitude of a single strong A_{1g} mode (identified from the Ritz analysis) as a guide; 6) performing EMAR measurements with each of the electrode configurations; 7) pairing each of the significant EMAR peak frequencies with the closest matching RUS frequency; and 8) comparing the symmetries of the modes determined by Ritz analysis of the RUS data with the expected modal symmetries listed in Table II for EMAR.

V. RESULTS

RUS measurements of resonant frequencies of the quartz specimen were performed at ambient temperatures

TABLE III
ELASTIC CONSTANTS (GPa) OF QUARTZ DETERMINED BY
BECHMANN [7] AND IN THIS STUDY BY RITZ ANALYSIS OF RUS
DATA.

	C_{11}	C_{33}	C_{44}	C_{12}	C_{13}	C_{14}
This study	87.16	105.8	58.34	6.69	12.02	−18.20
Bechmann [17]	86.74	107.2	57.94	6.98	11.91	−17.91

TABLE IV
MODAL SYMMETRY (IR), CALCULATED FREQUENCY f_{CAL}, RUS
FREQUENCY f_{RUS}, EMAR FREQUENCY f_{EMAR}, EMAR
CONFIGURATION IN WHICH EACH PEAK IS SIGNIFICANT, AND
FRACTIONAL DIFFERENCE IN EXPERIMENTAL FREQUENCIES
$\Delta f/f \equiv (f_{\text{RUS}} - f_{\text{EMAR}})/f_{\text{EMAR}})$ FOR MODES WITH A_{1g}, A_{2g}, OR A_{1u}
SYMMETRY BELOW 0.600 MHz.*

IR	f_{cal}	f_{rus}	f_{emar}	Config.	$\Delta f/f$
A_{1u}	0.143542	0.143646	—	—	—
A_{1g}	0.204860	0.204974	—	—	—
A_{2g}	0.280852	0.281132	0.280854	D	0.0010
A_{1g}	0.286056	0.286187	—	—	—
A_{1g}	0.319607	0.319623	0.319510	E	0.0004
A_{1u}	0.359310	0.359820	0.359718	A	0.0003
A_{1g}	0.365205	0.364276	—	—	—
A_{2g}	0.368648	0.369177	0.369081	C,D	0.0003
A_{1g}	0.392141	0.391593	—	—	—
A_{1u}	0.407157	0.408503	0.408492	A,B	0.0000
A_{1u}	0.422937	0.423144	0.423022	A,B	0.0003
A_{2g}	0.430285	0.431062	0.430986	C,D	0.0002
A_{1g}	0.440131	0.439784	——	—	——
A_{2g}	0.482148	0.482364	0.482055	C,D	0.0006
A_{1u}	0.489834	0.490186	0.490026	A,B	0.0003
A_{1u}	0.537979	0.538021	0.537795	A,B	0.0014
A_{2g}	0.538701	0.538528	0.538391	C,D	0.0003
A_{1g}	0.540192	0.539491	—	—	—
A_{1g}	0.566885	0.565676	—	—	—
A_{2g}	0.573919	0.573496	0.573301	C,D	0.0003

*EMAR peaks with heights < 0.01 are not included. Frequencies are
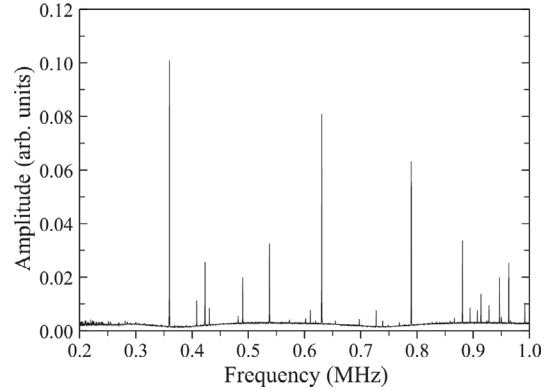in MHz.
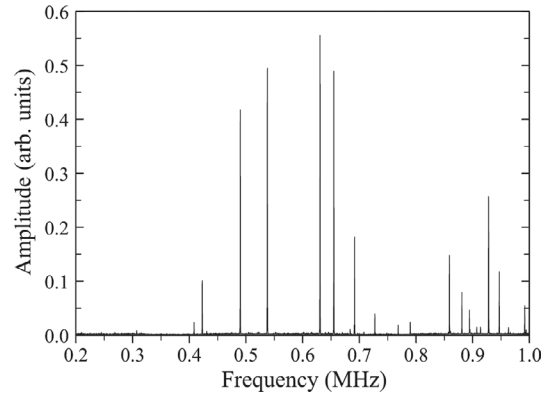

Fig. 3. Resonant spectrum for configuration *A*.

Fig. 4. Resonant spectrum for configuration *B*.

The elastic constants C_{ij} determined from the Ritz
analysis are listed in Table III. Our values for the C_{ij} are
consistent with the range of values for quartz that are re-
ported in the literature [19]. They are presented here for
the sake of completeness, but the central goal of the present
study is the demonstration of the mode-selective EMAR
technique, rather than accurate determination of C_{ij} with
RUS. More complete analysis would include piezoelectric
perturbations to the frequencies in the Ritz calculation,
and this is not pursued here.

Figs. 3–7 show resonant spectra acquired with the five
EMAR configurations *A–E* at ambient temperatures and
atmospheric pressure. The baseline noise in these spectra
is in the range of 0.002–0.003. Table IV lists the frequencies
f_{emar} of all EMAR modes detected below 0.600 MHz with
peak heights greater than 0.01 (approximately four times
the noise level). These frequencies are entered in this table
in the row of the most closely matching RUS frequencies.
The last column of Table IV lists the fractional differences
$\Delta f/f$ between the measured RUS and EMAR frequencies.

Uncertainties in the frequencies at constant tempera-
ture in both RUS and EMAR were on the order of a few
hertz. However, day-to-day variations in ambient temper-
atures were found to introduce variations in measured fre-
quencies on the order of 10–20 Hz. These temperature-
induced variations are significantly less than most of the
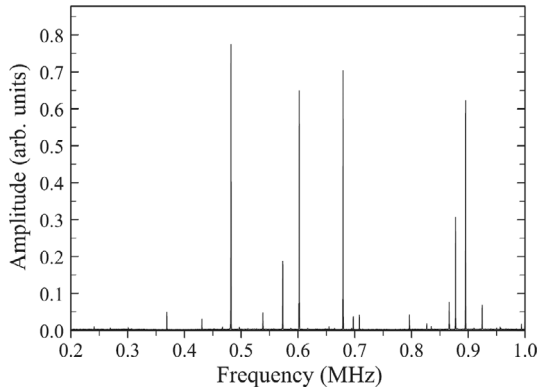differences in frequencies of RUS and EMAR listed in Ta-
ble IV.

(near 22°C) in a roughing vacuum of approximately 0.2 Pa.
Initial values of the elastic constants in the Ritz analy-
sis of these measurements were those of Bechmann [17],
which are listed in Table III. The density was fixed at
$2649.7 \pm 0.2 \text{ kg/m}^3$, which was determined by Archimedes'
method [18] using distilled water as a standard. The ini-
tial forward Ritz calculation with these values indicated
a one-to-one correlation with measured RUS frequencies
below 0.600 MHz. The subsequent Ritz inversion analy-
sis of the RUS data over this frequency range also was
consistent with this correlation, with an rms difference of
0.11% between the calculations and measurements. Ta-
ble IV presents the calculated frequencies f_{cal} and mea-
sured RUS frequencies f_{rus} for modes with A_{1u}, A_{2g}, or
A_{1g} symmetry. Although only modes with these symme-
tries are presented in this table, all ninety RUS frequencies
below 0.600 MHz were used in the inversion analysis, in-
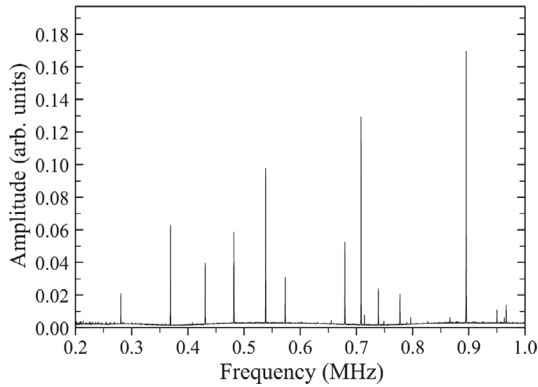cluding those with A_{2u}, E_g, and E_u symmetry.

Fig. 5. Resonant spectrum for configuration C.

Fig. 6. Resonant spectrum for configuration D.

Table V presents forward Ritz calculations of modes of all symmetries between 0.59 and 0.64 MHz using the above C_{ij} determined from the inversion analysis of frequencies below 0.600 MHz. This table illustrates the types of problems in mode identification that can occur in Ritz analysis of RUS data, as described in the next section. The three EMAR frequencies in this table are paired with the closest calculated modes having the symmetry expected from the EMAR configurations (instead of being paired with the closest RUS frequency, as in Table IV).
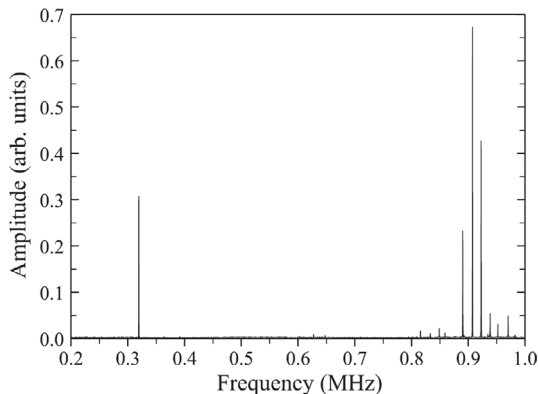

Fig. 7. Resonant spectrum for configuration E.

TABLE V

MODAL SYMMETRY (IR), CALCULATED FREQUENCY f_{CAL}, RUS FREQUENCY f_{RUS}, EMAR FREQUENCY f_{EMAR}, EMAR CONFIGURATION IN WHICH EACH PEAK IS SIGNIFICANT, AND FRACTIONAL DIFFERENCE IN EXPERIMENTAL FREQUENCIES $\Delta f/f \equiv (f_{\text{RUS}} - f_{\text{EMAR}})/f_{\text{EMAR}}$ FOR MODES WITH ALL SYMMETRIES BETWEEN 0.591 MHz AND 0.640 MHz.*

IR	f_{cal}	f_{rus}	f_{emar}	Config.	$\Delta f/f$
E_g	0.591228	0.591278	—	—	—
	0.591228	0.591354	—	—	—
E_g	0.597143	0.596599	—	—	—
	0.597143	0.596783	—	—	—
E_u	0.600455	0.599477	—	—	—
	0.600455	0.599727	—	—	—
A_{2g}	0.602264	0.602064	0.602276	C	-0.0004
E_u	0.602633	0.602592	—	—	—
	0.602633	0.602731	—	—	—
A_{1g}	0.604852	0.603262	—	—	—
E_g	0.608025	0.607137	—	—	—
	0.608025	0.607710	—	—	—
A_{1u}	0.609445	0.608173	—	—	—
E_u	0.609757	0.609384	—	—	—
	0.609757	0.609662	—	—	—
A_{2u}	0.609804	0.610629	—	—	—
E_u	0.619425	0.618912	—	—	—
	0.619425	0.619730	—	—	—
E_g	0.623708	0.623186	—	—	—
	0.623708	0.623434	—	—	—
A_{1g}	0.627528	0.626825	0.627404	E	-0.0009
E_u	0.628368	0.627035	—	—	—
	0.628368	0.627421	—	—	—
E_g	0.629105	0.627553	—	—	—
	0.629105	0.627664	—	—	—
A_{1u}	0.630672	0.631089	0.630772	A, B	0.0005
A_{1g}	0.637569	0.636784	—	—	—

*EMAR peaks with heights < 0.01 are not included. Frequencies are in MHz.

VI. DISCUSSION

In Table IV, the symmetries of the modes determined through the Ritz analysis correspond exactly to the symmetries expected from Table II for each of the EMAR configurations. A few weaker EMAR peaks with heights less than 0.01 (not included in Table IV) correspond to calculated modes with symmetries that do not match expectations. These modes include ones with A_{2g} symmetry that were weakly detected in configuration A (contrary to the expectation from Table II) but strongly detected in configurations C and D (consistent with Table II). The slight coupling to these modes in configuration A may arise from imperfections in the symmetry of the electrodes.

EMAR has not detected all vibrational modes below 0.600 MHz with A_{1g} symmetry, as indicated by the dashed lines in Table IV. The lack of detection of these modes is understood to arise from features of the displacement patterns that are not included in the general categorization of the modes according to group theory. As described by Johnson and Heyliger [14], A_{1g} modal displacement patterns can be described by Ritz approximation functions with a number of different detailed symmetries for the

azimuthal, radial, and axial components of the displacements. The specific configuration E couples only to a subset of these modes. For example, the three-fold symmetry of configuration E is not expected to couple significantly to the lowest-frequency A_{1g} mode near 0.205 MHz because of weak azimuthal variation of the displacements of this mode. This expectation is based on the calculations of Heyliger and Johnson [13], which show weak azimuthal variation for the lowest A_{1g} mode of a langatate cylinder (with the orientation of the three-fold crystallographic axis the same as that of the quartz specimen in the present study).

The lowest A_{1u} mode (near 0.144 MHz) also is absent in the EMAR spectra. This mode is not expected in the spectra, because the low-frequency limit of the electronics is approximately 0.20 MHz.

The relative sparseness of the EMAR spectra is not expected to be a limitation with respect to accurately determining C_{ij} through Ritz inversion analysis. The Ritz analysis indicates that the set of A_{1u} and A_{2g} modes detected in EMAR includes significant sensitivity to each of the C_{ij}. Also, similarly sparse spectra have successfully been used in previous studies to extract values of C_{ij} that are consistent with those extracted from full RUS spectra [8], [12].

The measured RUS frequencies in Table IV are slightly higher (by 0.02 to 0.14%) than the corresponding EMAR frequencies, with the exception of 0.4085 MHz, which is almost identical. Increases in frequencies are expected from the perturbation of stress-free boundaries introduced by mechanical contact of transducers in RUS measurements, and such increases have been reported in previous studies that directly compared RUS and EMAR results [8], [12]. Systematic differences in sample temperature during the RUS and EMAR measurements (arising, for example, from slight resistive heating of the sample in EMAR) also may contribute to the observed differences in frequency.

Difficulties in RUS mode identification become apparent in the extension of forward Ritz calculations above 0.600 MHz (Table V). For example, the difference in frequency of the calculated A_{2g} and E_u modes at 0.602264 and 0.602633 is comparable to the listed difference in f_{rus} of the doubly degenerate E_u modes (which arises from imperfections in the geometry or crystal alignment of the specimen). Therefore, if the inverse calculation were extended into this frequency range, simply pairing calculated and measured RUS frequencies in sequence (as in Table V) might be incorrect. In fact, the negative value for $\Delta f/f$ of the A_{2g} mode in Table V suggests that such pairing is incorrect in this case, since the lower modes in Table IV show only positive values of $\Delta f/f$. An alternate identification of the A_{2g} mode with the RUS modes at either 0.602592 or 0.602731 MHz would make $\Delta f/f$ equal to 0.0005 or 0.0008, respectively, and these values are more consistent with those in Table VI. A similar situation occurs with the A_{1g} and E_u modes near 0.628 MHz, where an even larger negative value for $\Delta f/f$ results from sequential pairing of the RUS and calculated frequencies. The final A_{1u} mode in

Table V has a greater difference in frequency from adjacent modes, so that the RUS mode identification is more clear, and the value of $\Delta f/f$ with sequential pairing of calculations and RUS measurements falls back in line with values in Table IV.

VII. CONCLUSION

This work provides an experimental basis for determining elastic and piezoelectric constants of trigonal piezoelectric crystals from noncontacting mode-selective measurements on a single cylindrical specimen. It provides the first demonstration of a method for switching the coupling between resonant modes belonging to different group-theoretical irreducible representations simply by switching the leads to a single set of electrodes. It demonstrates and analyzes the selectivity of the transduction technique with respect to modal symmetry, while leaving to subsequent research the logical next step of determining the elastic and piezoelectric constants through Ritz inversion analysis of the EMAR measurements.

Ritz inversion analysis of RUS data has been employed here as a means of demonstrating the modal selectivity of the EMAR technique. Potential problems with incorrect pairing of calculated frequencies and RUS frequencies have been avoided by limiting the analysis to a frequency range over which there is no apparent uncertainty in modal identification, a practice that is standard among RUS practitioners. Difficulties in determining the correspondence of calculated and measured RUS modes at higher frequencies have been considered only for the purposes of illustration. However, the situation described here is a best-case scenario in which initial guesses for the elastic constants are relatively good because of previously published results from many studies that employed a variety of acoustic techniques. In cases where little or no published information on the elastic constants is available, the frequency range over which RUS modal identification is unambiguous can be inadequate for effective inversion analysis. Difficulties in identification also arise in measurements performed as a function of temperature, even in fairly well characterized materials, since modes of different symmetry often become nearly degenerate at certain temperatures.

The principal application that is targeted in this study is the simultaneous measurement of elastic and piezoelectric constants as a function of temperature in innovative materials for frequency-control and sensing applications. For such measurements, the technique presented here has several advantages relative to RUS and other conventional acoustic methods. Because the transduction is noncontacting, it minimizes perturbations to the frequencies, which are particularly critical in the extraction of piezoelectric constants. It maintains the RUS advantage of providing information on all of the elastic and piezoelectric constants from measurements on one specimen in a single orientation. At the same time, it provides selectivity in the excitation and detection of acoustic modes, which eliminates

TABLE VI
Effect of Symmetry Transformations on Coordinates and
Factors Multiplying Unit Vectors.

	ϕ	z	$\hat{\phi}$	$\hat{z}$
E	ϕ	z	$\hat{\phi}$	$\hat{z}$
C_{3z}	$\phi + 2\pi/3$	z	$\hat{\phi}$	$\hat{z}$
C_{3z}^{-1}	$\phi - 2\pi/3$	z	$\hat{\phi}$	$\hat{z}$
C_{2x}	$-\phi$	$-z$	$-\hat{\phi}$	$-\hat{z}$
C_{2f}	$-\phi + 4\pi/3$	$-z$	$-\hat{\phi}$	$-\hat{z}$
C_{2d}	$-\phi - 4\pi/3$	$-z$	$-\hat{\phi}$	$-\hat{z}$
C_I	$-\phi + \pi$	$-z$	$\hat{\phi}$	$-\hat{z}$

potential difficulties in modal identification at all temperatures.

Appendix A
Symmetry Analysis

This appendix presents analysis of the symmetries of the potential V, electric field $\vec{E}$, and strain field S in a trigonal crystal with cylindrical geometry surrounded by each of the configurations of electrodes shown in Fig. 2. For a given configuration, the symmetry of the induced strain field belongs to one of the one-dimensional irreducible representations of the D_{3d} point group, and resonant acoustic modes with these symmetries are excited if the potential varies at the corresponding resonant frequency.

Within the present context of spatial transformations, the elements g_i of the group D_{3d} are identified with transformations $R(g_i)$ of coordinate axes [15]. For example, C_{3z} is a rotation of the coordinate axes by $2\pi/3$ performed in the right-hand screw sense about $\hat{z}$. Corresponding to each of the coordinate-transformation operators is an operator $P(g_i)$ that acts on functions. Following the usual Wigner convention [20], the $P(g_i)$ rotate contours of functions in the opposite direction to the corresponding rotation of coordinate axes, so that, for scaler functions $f(\vec{r})$ of position $\vec{r}$,

$$P(g_i)f(\vec{r}) = f(R^{-1}\vec{r}). \tag{A1}$$

Therefore, scalar functions are transformed under the symmetry operations of D_{3d} by substituting, for the coordinates ϕ and z, the entries listed under the corresponding columns in Table VI. (The coordinate r is unchanged by the symmetry operations.) Transformations of expressions for vector fields also include these substitutions and, in addition, the introduction of factors of 1 or -1 multiplying the unit vectors $\hat{\phi}$ and $\hat{z}$, according to the last two columns of Table VI [14].

In the absence of the specimen, the potential is given by

$$V(r,\phi,z,t) = V_0(r,\phi,z)f(t), \tag{A2}$$

where $f(t)$ is proportional to the gated RF voltage applied to the electrodes. Therefore, the symmetry of V in each of

the electrode configurations is that of the corresponding image in Fig. 2 (considering the polarities indicated by the shading), which is easily determined by inspection. In configuration C, for example,

$$\begin{aligned}
P(C_{3z})V_0(r,\phi,z) &= V_0(r,\phi + 2\pi/3,z) \\
&= V_0(r,\phi,z), \\
P(C_{3z}^{-1})V_0(r,\phi,z) &= V_0(r,\phi - 2\pi/3,z) \\
&= V_0(r,\phi,z), \\
P(C_{2x})V_0(r,\phi,z) &= V_0(r,-\phi,-z) \\
&= -V_0(r,\phi,z), \\
P(C_{2f})V_0(r,\phi,z) &= V_0(r,-\phi + 4\pi/3,-z) \\
&= -V_0(r,\phi,z), \\
P(C_{2d})V_0(r,\phi,z) &= V_0(r,-\phi - 4\pi/3,-z) \\
&= -V_0(r,\phi,z), \\
P(C_I)V_0(r,\phi,z) &= V_0(r,-\phi + \pi,-z) \\
&= -V_0(r,\phi,z)\hat{z}.
\end{aligned} \tag{A3}$$

Therefore, V in this configuration is a basis for A_{2u}. V in each of the other configurations similarly can be shown to transform according to the IRs listed in Table II.

The applied electric field $\vec{E}$ is given by

$$\begin{aligned}
\vec{E} &= \vec{E}_0(r,\phi,z)f(t) \\
&= [E_r(r,\phi,z)\hat{r} + E_\phi(r,\phi,z)\hat{\phi} + E_z(r,\phi,z)\hat{z}]f(t) \\
&= -\nabla V \\
&= -\frac{\partial V}{\partial r}\hat{r} - \frac{1}{r}\frac{\partial V}{\partial \phi}\hat{\phi} - \frac{\partial V}{\partial z}\hat{z}.
\end{aligned} \tag{A4}$$

From Table VI and (A3) and (A4), the transformation of $\vec{E}$ under C_{2x} in configuration C is given by

$$\begin{aligned}
P(C_{2x})\vec{E}_0(r,\phi,z) &= -\frac{\partial V_0(r,-\phi,-z)}{\partial r}\hat{r} \\
&\quad + \frac{1}{r}\frac{\partial V_0(r,-\phi,-z)}{\partial(-\phi)}\hat{\phi} \\
&\quad + \frac{\partial V_0(r,-\phi,-z)}{\partial(-z)}\hat{z} \\
&= \frac{\partial V_0(r,\phi,z)}{\partial r}\hat{r} \\
&\quad + \frac{1}{r}\frac{\partial V_0(r,\phi,z)}{\partial \phi}\hat{\phi} \\
&\quad + \frac{\partial V_0(r,\phi,z)}{\partial z}\hat{z} \\
&= -\vec{E}_0(r,\phi,z).
\end{aligned} \tag{A5}$$

Similarly, $\vec{E}$ can be shown to transform in the same manner as V under all of the symmetry operations in each of the configurations, as summarized in Table II.

The fact that $\vec{E}_0$ transforms according to the same IR as V_0 can be demonstrated more generally and succinctly in the language of differential forms [21]. The electric field is a 1-form that is defined by

$$E_0 = -d_\wedge V_0, \tag{A6}$$

where $d_\wedge$ denotes the exterior derivative. The operators $P(g_i)$ are pull-backs, which commute with the exterior derivative [21]. Therefore, the transformations of E_0 are given by

$$\begin{aligned} P(g_i)E_0 &= -P(g_i)^\star d_\wedge V_0 \\ &= -d_\wedge[P(g_i)^\star V_0]. \end{aligned} \quad (A7)$$

The equivalence of the transformation properties of $\vec{E}_0$ and V_0 are fairly transparent in this equation. In the case of a one-dimensional IR, the changes in sign of V_0 under each of the g_i results in the same change in sign of $\vec{E}_0$.

In the absence of an applied stress, the components of strain S that are piezoelectrically induced by a time-independent electric field are given by the electromechanical constitutive equation [22],

$$[S] = \begin{bmatrix} d_{11}\cos 3\phi & -d_{11}\sin 3\phi & 0 \\ -d_{11}\cos 3\phi & d_{11}\sin 3\phi & 0 \\ 0 & 0 & 0 \\ d_{14} & 0 & 0 \\ 0 & -d_{14} & 0 \\ -2d_{11}\sin 3\phi & -2d_{11}\cos 3\phi & 0 \end{bmatrix} \begin{bmatrix} E_r \\ E_\phi \\ E_z \end{bmatrix}. \quad (A8)$$

The conventional contracted notation in cylindrical coordinates is used here for the components of S: $S_1 \equiv S_{rr}$, $S_2 \equiv S_{\phi\phi}$, $S_3 \equiv S_{zz}$, $S_4 \equiv S_{\phi z}$, $S_5 \equiv S_{rz}$, and $S_6 \equiv S_{r\phi}$) [22]. Eq. (A8) can be expressed in dyadic notation as

$$\begin{aligned} S &= [E_r d_{11}\cos 3\phi - E_\phi d_{11}\sin 3\phi]\hat{r}\hat{r} \\ &+ [-E_r d_{11}\cos 3\phi + E_\phi d_{11}\sin 3\phi]\hat{\phi}\hat{\phi} \\ &+ [E_r d_{14}]\hat{\phi}\hat{z} - [E_\phi d_{14}]\hat{r}\hat{z} \\ &+ [-E_r d_{11}\sin 3\phi - E_\phi d_{11}\cos 3\phi]\hat{r}\hat{\phi}. \end{aligned} \quad (A9)$$

Applying each of the symmetry transformations (Table VI) to (A9) and using the results for $\vec{E}$ summarized in Table II, S is found to transform in the same manner as V and $\vec{E}$, except that the inversion symmetry is reversed.

With electric fields driven at a frequency near an acoustic resonance, the strains in the material will be larger than those given by the time-independent analysis of S, above, and the detailed spatial dependence will be determined predominantly by the resonant modal displacement patterns. However, the general symmetries (IRs) of the resonantly driven strains will be the same as in the time-independent case.

REFERENCES

[1] A. Migliori and J. Sarrao, *Resonant Ultrasound Spectroscopy.* New York: Wiley, 1997.

[2] H. Ogi, Y. Kawasaki, M. Hirao, and H. Ledbetter, "Acoustic spectroscopy of lithium niobate: Elastic and piezoelectric coefficients," *J. Appl. Phys.*, vol. 92, pp. 2451–2456, 2002.

[3] J. Schreuer, "Elastic and piezoelectric properties of $La_3Ga_5SiO_{14}$ and $La_3Ga_{5.5}Ta_{0.5}O_{14}$: An application of resonant ultrasound spectroscopy," *IEEE Trans. Ultrason., Ferroelect., Freq. Contr.*, vol. 49, pp. 1474–1479, 2002.

[4] H. Ogi, N. Nakamura, K. Sato, M. Hirao, and S. Uda, "Elastic, anelastic, and piezoelectric coefficients of langasite: Resonance ultrasound spectroscopy with laser-Doppler interferometry," *IEEE Trans. Ultrason., Ferroelect., Freq. Contr.*, vol. 50, pp. 553–560, 2003.

[5] H. Ledbetter, H. Ogi, and N. Nakamura, "Elastic, anelastic, and piezoelectric coefficients of monocrystal lithium niobate," *Mech. Mater.*, vol. 36, pp. 941–947, 2004.

[6] H. Ogi, T. Ohmori, N. Nakamura, and M. Hirao, "Elastic, anelastic, and piezoelectric coefficients of α-quartz determined by resonance ultrasound spectroscopy," *J. Appl. Phys.*, vol. 100, art. no. 053511, 2006.

[7] I. Ohno, "Rectangular parallelepiped resonance method for piezoelectric crystals and elastic constants of alpha-quartz," *Phys. Chem. Miner.*, vol. 17, pp. 371–378, 1990.

[8] H. Ogi, H. Ledbetter, S. Kim, and M. Hirao, "Contactless mode-selective resonance ultrasound spectroscopy: Electromagnetic acoustic resonance," *J. Acoust. Soc. Amer.*, vol. 106, pp. 660–665, 1999.

[9] H. Ogi, K. Sato, T. Asada, and M. Hirao, "Complete mode identification for resonance ultrasound spectroscopy," *J. Acoust. Soc. Amer.*, vol. 112, pp. 2553–2557, 2002.

[10] H. Ogi, M. Fukunaga, M. Hirao, and H. Ledbetter, "Elastic constants, internal friction, and piezoelectric coefficient of α-TeO$_2$," *Phys. Rev. B*, vol. 69, art. no. 024104, 2004.

[11] M. Hirao and H. Ogi, *EMATS for Science and Industry: Noncontacting Ultrasonic Measurements.* Boston: Kluwer Academic, 2003.

[12] H. Ogi, P. Heyliger, H. Ledbetter, and S. Kim, "Mode-selective resonance ultrasound spectroscopy of a layered parallelepiped," *J. Acoust. Soc. Amer.*, vol. 108, pp. 2829–2834, 2000.

[13] P. Heyliger and W. Johnson, "Traction-free vibrations of finite trigonal elastic cylinders," *J. Acoust. Soc. Amer.*, vol. 113, pp. 1812–1825, 2003.

[14] W. Johnson and P. Heyliger, "Symmetrization of Ritz approximation functions for vibrational analysis of trigonal cylinders," *J. Acoust. Soc. Amer.*, vol. 113, pp. 1826–1832, 2003.

[15] J. F. Cornwell, *Group Theory in Physics, Vol. I.* New York: Academic, 1984.

[16] W. Johnson, B. A. Auld, and G. A. Alers, "Spectroscopy of resonant torsional modes in cylindrical rods using electromagnetic-acoustic transduction," *J. Acoust. Soc. Amer.*, vol. 95, pp. 1413–1418, 1994.

[17] R. Bechmann, "Elastic and piezoelectric constants of quartz," *Phys. Rev.*, vol. 110, pp. 1060–1061, 1958.

[18] F. Spieweck and H. Bettin, "Review: Solid and liquid density determination," *Technisches Messen*, vol. 59, pp. 285–292, 1992.

[19] A. Ballato, "Elastic properties of crystalline quartz," in *Handbook of Elastic Properties of Solids, Liquids, and Gases.* vol. II, M. Levy, H. E. Bass, and R. R. Stern, Eds. New York: Academic, 2001, pp. 257–279.

[20] M. Tinkham, *Group Theory and Quantum Mechanics.* New York: McGraw-Hill, 1964, p. 32.

[21] T. Frankel, *The Geometry of Physics.* Cambridge, UK: Cambridge University Press, 1997.

[22] B. A. Auld, *Acoustic Fields and Waves in Solids.* Malabar, FL: Krieger, 1990.

Ward Johnson is a physicist with a background primarily in elastic and anelastic properties of materials. He is a graduate of the Physics Department of the University of Illinois at Urbana-Champaign with a Ph.D. thesis that was focused on anelastic effects of irradiation-induced point defects in semiconductors. In 1987, he joined the Metallurgy Division of the National Institute of Standards and Technology (NIST; Gaithersburg, Maryland) and, in 1994, transferred to the Materials Reliability Division of NIST in Boulder, Colorado. His work at NIST has included the development and application of metrology for characterizing mechanical and magnetic properties of macroscopic and nanoscale materials using electromagnetic-acoustic transduction, pulsed-laser acoustics, and Brillouin light scattering.

Carlos Martino received his bachelor's degree in physics with a minor in mathematics from the University of Houston, Texas, in 2002. Thereafter, he moved to Boulder, Colorado, and obtained a master's degree in mechanical engineering from the University of Colorado at Denver in 2004 and a master's degree in mathematics from the University of Colorado at Boulder in 2007. Currently, he is finishing a doctorate program in bioengineering at the University of Colorado at Boulder, while his research investigations are underway at the Technical University of Munich, Germany, under the supervision of Dr. Erich Wintermantel.

Paul Heyliger was awarded his Ph.D. degree in engineering science and mechanics from Virginia Tech in 1986. He joined the Civil Engineering Department at Colorado State University in 1988 following a two-year postdoctoral appointment at the National Bureau of Standards in Boulder, Colorado. He has held visiting professor and visiting researcher appointments at NASA-Lewis Research Center, the University of California at Santa Barbara, and the University of Stuttgart, Germany. He is currently Professor of Civil and Environmental Engineering at Colorado State University, where he studies computational mechanics of materials and structures.
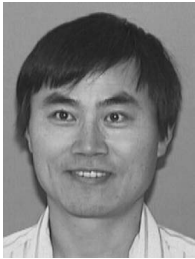
Sudook A. Kim received B.S. degrees in chemical engineering and applied mathematics from the University of Colorado at Boulder, Colorado, in 1984. He received an M.S. degree in engineering mechanics from the University of Colorado at Boulder in 1986. Since 1984, he has worked at the National Institute of Standards and Technology (NIST; formerly the National Bureau of Standards) in Boulder, Colorado. His research interests include elastic properties, internal friction, specific heat, magnetic properties, Debye temperatures, and low-temperature physical properties. His current research involves Brillouin light scattering and resonant ultrasound spectroscopy.